ACS APPLIED MATERIALS & INTERFACES

Research Article

Cite This: ACS Appl. Mater. Interfaces XXXX, XXX, XXX−XXX

www.acsami.org

Tuning ZnO Sensors Reactivity toward Volatile Organic Compounds via Ag Doping and Nanoparticle Functionalization

Vasile Postica,[†] Alexander Vahl,[‡] David Santos-Carballal,[*,⊥] Torben Dankwort,[§] Lorenz Kienle,[§] Mathias Hoppe,[∥] Abdelaziz Cadi-Essadek,[⊥] Nora H. de Leeuw,[*,⊥,#] Maik-Ivo Terasa,[∥] Rainer Adelung,[*,∥] Franz Faupel,[*,‡] and Oleg Lupan[*,†,∥]

[†]Center for Nanotechnology and Nanosensors, Department of Microelectronics and Biomedical Engineering, Technical University of Moldova, 168 Stefan cel Mare Av., MD-2004 Chisinau, Republic of Moldova

[‡]Chair for Multicomponent Materials, Faculty of Engineering, Institute for Materials Science, [§]Synthesis and Real Structure, Institute for Materials Science, and [∥]Functional Nanomaterials, Institute for Materials Science, Kiel University, Kaiserstr. 2, D-24143, Kiel, Germany

[⊥]School of Chemistry, Cardiff University, Main Building, Park Place, Cardiff CF10 3AT, United Kingdom

[#]Department of Earth Sciences, Utrecht University, Princetonplein 8A, 3584 CD Utrecht, The Netherlands

Supporting Information

ABSTRACT: Nanomaterials for highly selective and sensitive sensors toward specific gas molecules of volatile organic compounds (VOCs) are most important in developing new-generation of detector devices, for example, for biomarkers of diseases as well as for continuous air quality monitoring. Here, we present an innovative preparation approach for engineering sensors, which allow for full control of the dopant concentrations and the nanoparticles functionalization of columnar material surfaces. The main outcome of this powerful design concept lies in fine-tuning the reactivity of the sensor surfaces toward the VOCs of interest. First, nanocolumnar and well-distributed Ag-doped zinc oxide (ZnO:Ag) thin films are synthesized from chemical solution, and, at a second stage, noble nanoparticles of the required size are deposited using a gas aggregation source, ensuring that no percolating paths are formed between them. Typical samples that were investigated are Ag-doped and Ag nanoparticle-functionalized ZnO:Ag nanocolumnar films. The highest responses to VOCs, in particular to $(CH_3)_2CHOH$, were obtained at a low operating temperature (250 °C) for the samples synergistically enhanced with dopants and nanoparticles simultaneously. In addition, the response times, particularly the recovery times, are greatly reduced for the fully modified nanocolumnar thin films for a wide range of operating temperatures. The adsorption of propanol, acetone, methane, and hydrogen at various surface sites of the Ag-doped Ag_8/ZnO(0001) surface has been examined with the density functional theory (DFT) calculations to understand the preference for organic compounds and to confirm experimental results. The response of the synergistically enhanced sensors to gas molecules containing certain functional groups is in excellent agreement with density functional theory calculations performed in this work too. This new fabrication strategy can underpin the next generation of advanced materials for gas sensing applications and prevent VOC levels that are hazardous to human health and can cause environmental damages.

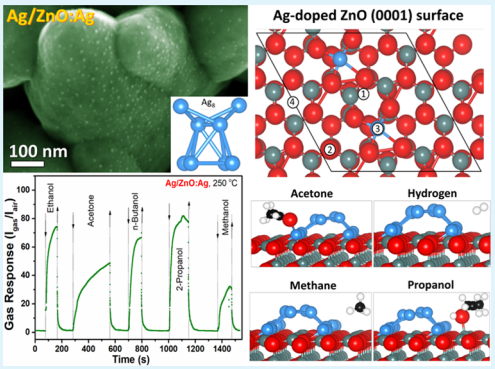

KEYWORDS: *columnar films, VOC sensors, DFT, surface functionalization, Ag nanoparticles*

1. INTRODUCTION

Advanced nanomaterials for gas sensing applications that have been traditionally used to detect volatile organic compound (VOC) levels, which are hazardous to human health and can cause environmental damages, are of high demand. However, a renewed and important interest in sensing nanomaterials has been driven by future applications in the identification of VOCs as biomarkers at early stage diseases. It is known that VOCs detected in exhaled breath at the ppb level can be related to several diseases.[1] Conventional metal oxide sensors seldom offer reliable detection at such low levels and mostly cannot distinguish one VOC within a complex sample. Thus, an alternative strategy is required to fabricate new semiconducting oxide nanomaterials that are cost-effective, highly sensitive, and selective at the same time, allowing integration into a small portable device.

Zinc oxide (ZnO) has a great potential for a wide range of applications, such as short-wavelength optoelectronics, photo-

Received: April 25, 2019
Accepted: July 23, 2019
Published: July 23, 2019

catalysis, VOC and gas sensing, and UV detection among others.[2−5] The main advantages of ZnO micro and nanostructures are their semiconducting and piezoelectric properties, biocompatibility (structure- and concentration-dependent), and the possibility to grow this material in a wide range of morphologies.[2] However, pure ZnO micro and nanostructures lack selectivity to specific gases, and the sensing properties are highly reduced by environmental humidity, which has led to a number of studies focused on overcoming these disadvantages.[6,7] In this context, doping and/or surface functionalization/decoration with different noble metals was found to be very efficient in improving the selectivity and sensitivity of ZnO while reducing the influence of water vapors on the sensing properties.[6,8−10]

According to the theory of valence control in oxide semiconductors,[11] the doping of ZnO with acceptor elements from the group I of the periodic table such as Li, K, Cu, and Ag decreases its Debye length (L_D).[11] The doping of ZnO enhances the modulation of the surface electron depletion region, favoring the surface adsorption and desorption of oxygen species, which increases the response to VOCs.[11−13] In particular, the Ag doping of ZnO micro and nanostructures/columns is a very attractive method to improve the sensing properties due to the excellent catalytic properties of Ag. The dopant atoms also generate additional adsorption sites for ambient oxygen, and the target gas molecules effectively promote the interaction between the substrate surface and the adsorbate.[12] For example, Ag nanoparticles have been successfully used alongside nanowire networks of stoichiometric[14] and nanoclusters of oxygen-deficient SnO_2 for the detection of ethanol.[15]

In this work, we show that synergistically enhancing metal oxide surfaces using doping and noble nanoparticle functionalization is a promising approach for engineering gas sensor materials. To demonstrate this new concept, the Ag-doped and Ag NP-decorated ZnO nanocolumnar films are investigated, over a wide range of operating temperatures, to determine experimentally which functionalization method is optimal for enhancing the gas sensing properties toward VOC vapors. A possible gas sensing mechanism is proposed and discussed in detail. In this study, we have also used quantum mechanical simulations to investigate the Ag doping and the decoration with Ag_8 clusters of the ZnO(0001) surface. We have evaluated the atomic charges and the electronic structure of different configurations to define the most stable geometry. Moreover, we have examined the adsorption of propanol, acetone, methane, and hydrogen at various surface sites of the Ag-doped Ag_8/ZnO(0001) to understand its preference for organic compounds.

2. EXPERIMENTAL SECTION

2.1. Synthesis of ZnO Nanocolumnar Thin Films. Ag-doped nanocolumnar ZnO films were grown on glass substrates to reduce possible budging. The glass substrates were cleaned and then sensitized as described in refs 16 and 17. Ag-doped nanocolumnar ZnO films were deposited on the substrates by the synthesis from chemical solution (SCS) method, as reported previously.[16−21] The thickness of the columnar films in this study was about 1.5 μm. The Ag contents used in the samples were 0.50, 0.95, and 1.3 wt %, which were achieved by adding 1.8, 5.3, and 12.3 mM silver nitrate ($AgNO_3$) in complex solution, respectively. The content of Ag was measured using energy-dispersive X-ray (EDX) spectroscopy. All samples were treated by rapid thermal annealing (RTA) at 475 °C (marked as RTA475), 575 °C (RTA575), and 725 °C (RTA725) for 60 s after deposition. More details on the SCS synthesis of doped ZnO columnar films are presented in our previous works.[16−21]

Silver nanoparticles (Ag NPs) were deposited onto the ZnO:Ag sensor layers with different densities via the gas-phase physical vapor deposition process based on a homemade[22,23] Haberland-type[24] gas aggregation cluster source and unipolar direct current (DC) planar magnetron sputtering. The target (Ag, Kurt J. Lesker, 99.99%, 5 cm diameter) was mounted onto a DC planar magnetron source (Thin Film Consulting, ION'X-2UHV). The base pressure of the HV deposition system prior to every deposition was below 10^{-4} Pa, using a two-stage pumping system (turbo molecular pump, Pfeiffer Vacuum, TMU 262; dry scroll pump, Agilent Technologies, SH-110). For the nanoparticle deposition, a flow of Ar (48SCCM, purity of 99.999%) was supplied at the gas inlet close to the target (gas regulating valve, Pfeiffer, EVR116 with attached hot ion cathode IMR 285), resulting in a pressure of typically 136 Pa during deposition. The DC power of 40 W was supplied by Advanced Energy, MDX 500. Prior to the deposition of nanoparticles, the Ag target was cleaned, and the nanoparticle growth was achieved by sputtering with closed shutter for a sufficient time (at least 30 s) to reach stable deposition conditions. After deposition, the samples were subjected to thermal annealing in air at 350 °C for 1 h.

The methodology details for the fabrication of the sensor structures are presented in previous works,[19,25] and the measurement of the gas sensing properties are presented in our publications.[18,26,27] The electrical measurements were performed using a Keithley 2400 sourcemeter with two-wire configuration through the LabVIEW software (National Instruments).[27] To form contacts, a thin layer of gold (Au, ∼170 nm) was sputtered on the surface of columnar films. The gap between contacts is ∼1 mm. The final structure of the device is Au/AgNPs/ZnO:Ag/Au.

2.2. Characterization of Materials. The ZnO:Ag/AgNP nanocomposite as well as its constituents, the ZnO:Ag base layer, and the deposited AgNP were investigated by X-ray photoelectron spectroscopy (XPS, Omicron NanoTechnology GmbH). The X-ray source was operated with an Al anode at a power of 240 W. All recorded spectra were charge-referenced by using aliphatic carbon C 1s at 285.0 eV using the software CasaXPS (version 2.3.16). (S)TEM analyses were performed using FEI Tecnai F30 G2 (FEG, 300 kV) equipped with a Si(Li) EDX detector (EDAX system).

2.3. Computational Details. We employed the Vienna ab initio simulation package (VASP),[28] which solves the Kohn−Sham equations of the density functional theory (DFT) in periodic conditions to simulate all geometries and energies.[29] All the calculations were spin-polarized, and the generalized gradient approximation (GGA) with the Perdew−Burke−Ernzerhof (PBE)[30] was adopted as the density functional. The semiempirical method of Grimme with the Becke−Johnson damping (DFT-D3-(BJ))[31] was considered to evaluate the long-range dispersion interactions. The *d* electrons of Zn and Ag were corrected using the Dudarev approach,[32] in the DFT + U[33] scheme, as implemented in the VASP software. Note that the U considered in this work corresponds to the effective Hubbard $U_{eff} = U - J$, where the exchange parameter J is equal to zero. We chose a U_{eff} value of 6.0 eV for both Ag[34] and Zn[27] atoms.

The electrons in the 4d5s orbitals of Ag, 3d4s of Zn, 2s2p of O as well as C, and 1s of H were treated as valence electrons. The projected augmented wave method (PAW)[35] was employed to describe the interaction between the atomic frozen core states and the valence electrons. The plane-wave basis set expansion was calculated by affixing the kinetic energy cutoff at 400 eV. We used the conjugate gradient technique with an ionic convergence criterion of 0.01 eV/Å for all geometry optimizations. We sampled the reciprocal space by adopting a Γ-centered 4 × 4 × 2 and 1 × 1 × 1 mesh of *k*-points for the ZnO bulk and ZnO(0001) surface, respectively. We also adopted a 1 × 1 × 1 mesh of *k*-points for the optimization of the molecules in the gas phase where each molecule was positioned in the center of a large box (20 × 21 × 22 Å^3) to avoid lateral interactions.

We considered the wurtzite structure of the ZnO bulk, which belongs to the space group $P6_3mc$ (no. 186). We optimized and described the ZnO bulk in our previous investigation.[20] We generated

DOI: 10.1021/acsami.9b07275
ACS Appl. Mater. Interfaces XXXX, XXX, XXX−XXX

the ZnO(0001) surface from the bulk using the METADISE[36] code, which takes into account the periodicity of the planes parallel to the surface and the atomic charges. To quench the dipole moment of the ZnO(0001) surface, we removed Zn atoms from the upper surface layer, similarly to previous investigations.[37]

Our ZnO(0001) surface is modeled by a 1 × 1 supercell, that is, containing two infinite surfaces at either side of the slab. A 20 Å of vacuum was added in the z direction to avoid interaction between neighboring cells. The ZnO(0001) slab contains four atomic layers (30 atoms) where the top two layers were allowed to relax during geometry optimization, and the bottom two layers were kept fixed at their equilibrium bulk position. The surface area is 35.49 Å^2 for the 1 × 1 supercell. We expanded our supercell to 2 × 1 and 2 × 2 slabs for Ag doping and Ag_8 clusters adsorption as well as the molecule adsorptions, respectively. The 2 × 1 slab has a surface area of 70.98 Å^2 and contains 60 atoms, while the 2 × 2 slab has a surface area of 141.97 Å^2 and contains 120 atoms.

To evaluate the interaction between the Ag_8 cluster and the Ag-doped ZnO(0001) surface, we calculated the clustering energy per Ag atom (E_{clus}) (eq 1)

$$E_{clus} = \frac{E_{Ag_8/surf} - (E_{surf} + 8E_{Ag})}{8} \quad (1)$$

where $E_{Ag_8/surf}$, E_{surf}, and E_{Ag} are the energies of the doped slab with the Ag_8 cluster, the clean doped oxide surface, and the Ag metal atom in the bulk, respectively, and 8 is the number of adsorbed Ag atoms. A positive clustering energy proves that the Ag atoms prefer to aggregate rather than spread over the surface, while a negative clustering energy indicates that the Ag atoms tend to wet the surface.

To describe the interaction of the molecules with the fully modified oxide surface, that is, Ag-doped and decorated with the Ag_8 cluster, we calculated the binding energy as (eq 2)

$$E_B = E_{molecule-surface} - (E_{surface} + E_{molecule}) \quad (2)$$

where $E_{molecule-surface}$ is the energy of the fully modified surface and the adsorbed molecule, while $E_{surface}$ and $E_{molecule}$ are the energies of the surface without the molecule and the isolated molecule, respectively. A positive binding energy is the consequence of an unfavorable endothermic adsorption, while a negative value indicates a favorable exothermic molecular adsorption.

We carried out the charge analysis of the system using the Bader atoms-in-molecules methodology as implemented in the Henkelman algorithm.[38]

3. RESULTS AND DISCUSSION

3.1. Morphological Characterization of Nanomaterials. Figure 1a–d shows the scanning electron microscopy (SEM) images of nanocolumnar ZnO:Ag films after rapid thermal annealing (RTA) at 575 °C with different Ag nominal concentrations (in wt %). All samples of pure and Ag-doped ZnO are composed of closely packed grains/columns forming thin films (see Figure S1). The column radius of the undoped samples lies between 100–250 nm, which decreases to 25–120 nm and 50–150 nm after doping with Ag at 0.50 and 0.95 wt %, respectively (see Figure 1a–c). However, a further increase in the Ag content to 1.3 wt % favors larger column radius of 70–220 nm (see Figure 1d). The column size histogram of ZnO:Ag with different Ag contents as a function of the RTA temperature is presented in Figure S2, showing the changes in column diameter.[18,19] Figure 1e–h and Figure S3 show the SEM images of Ag NP-functionalized ZnO:Ag samples, where the nanoscopic particles with different densities on the surface of the ZnO:Ag columns can be observed. In both cases, the NPs have a diameter of 6–12 nm and are well distributed on the surface of the ZnO:Ag columns/grains without a visible formation of percolating paths between NPs. The samples with

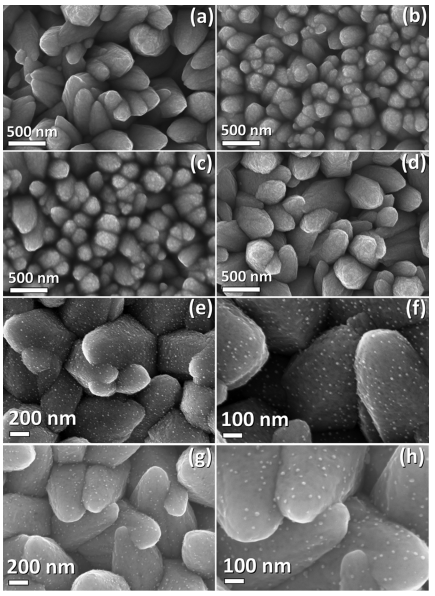

Figure 1. SEM images of columnar ZnO:Ag films after rapid annealing RTA at 575 °C for 60 s with: (a) 0.00, (b) 0.50, (c) 0.95, and (d) 1.30 wt % Ag content. SEM images of Ag-functionalized columnar ZnO:Ag films: (e, f) Ag(1)/ZnO:Ag and (g, h) Ag(2)/ZnO:Ag.

lower density of Ag NPs (~0.5 × 10^9 cm^{-2}; see Figure 1e,f) will be designated further as Ag(1)/ZnO:Ag, while samples with higher density of Ag NPs (~0.8 × 10^9 cm^{-2}; see Figure 1g,h) will be designated further as Ag(2)/ZnO:Ag.

3.2. Structural Characterization of Materials. The crystal structure and preferential orientation of the ZnO:Ag columnar films on the glass substrates were studied by X-ray diffraction (XRD). Figure 2a displays the XRD patterns for the pure and Ag-doped samples deposited using the synthesis from

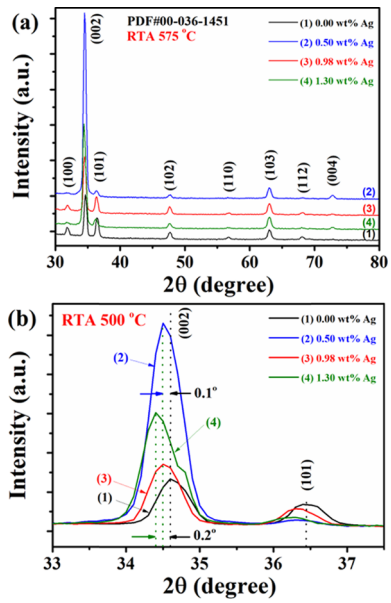

Figure 2. (a) XRD patterns of the columnar ZnO and ZnO:Ag films subjected to RTA at 575 °C for 60 s with different Ag contents. (b) Enlargement of the XRD pattern in the region between 2θ = 33 and 37.5° exhibit reflections corresponding to the (002) and (101) planes for the samples with different Ag concentrations.

DOI: 10.1021/acsami.9b07275
ACS Appl. Mater. Interfaces XXXX, XXX, XXX−XXX

chemical solution (SCS) method and subjected to the RTA at 575 °C for 60 s. The relatively low background intensity demonstrates good crystallinity of the ZnO samples, which can be assigned to the hexagonal wurtzite structure with space group $P6_3mc$ (no. 186). Figure 2a illustrates that the strongest detected (hkl) reflections are at expected 2θ values and correspond to the (100), (002), (101), (102), (110), (103), (112), and (004) Miller planes. We found an increase in the crystallinity by adding silver nitrate to the zinc complex solution during preparation of the ZnO:Ag film. A sharp (002) reflection at $2\theta \approx 34.6°$ with the highest observed intensity for the undoped ZnO shows a preferential growth along the c axis normal to the glass substrate.[18]

To gain insight into the effect of the various Ag concentrations on the crystallinity of the ZnO:Ag columnar films, we monitored the intensity of the (002) and (101) reflections (see Figure 2b). The XRD patterns indicate a shift to lower scattering angles (2θ, ~0.1°) for the samples with ~0.50 wt % Ag (curve 2) and ~0.95 wt % Ag (curve 3), while the highest Ag content of ~1.3 wt % (curve 4) induces a larger 2θ shift (~0.2°). It is the result of either the Ag ion interstitial incorporation into or Zn^{2+} substitution within the ZnO lattice[39] due to the 1.7 times larger ionic radii of Ag^{+} with respect to Zn^{2+}.[40] A similar lattice deformation was also observed for the Ag-doped ZnO thin films,[40] where the value of the 2θ angle shift increases with the Ag concentration.

Figure 3a depicts the high-resolution transmission electron microscopy (HRTEM) micrographs and fast Fourier transform

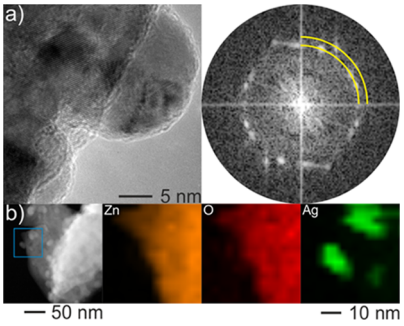

Figure 3. (a) HRTEM and FFT of one Ag nanoparticle attached to the ZnO surface. (b) High-angle annular dark-field (HAADF)-STEM and EDX elemental maps of the marked region.

(FFT) of nanoparticles attached to the surface of the single crystalline ZnO columnar matrix. The nanoparticle exhibited d spacing values of 2.30 and 2.04 Å corresponding to the crystal structure of cubic Ag. A clear epitaxial relation between the Ag nanoparticles and the ZnO matrix could not be observed. Bright atomic number-dependent contrast via high-angle annular dark-field scanning TEM (HAADF-STEM) exhibits Ag particles of 5−10 nm. The energy-dispersive X-ray (EDX) elemental maps verify the presence of nonoxidized Ag NPs attached to the ZnO columnar matrix surface.

3.3. Micro-Raman Characterization. The Raman spectra were measured at room temperature in the range between 60 and 1200 cm^{-1} to identify the influence of the Ag dopant on the columnar ZnO:Ag films (see Figure 4). Group theory predicts the optical phonons at the Γ point of the Brillouin zone and has the following representation[41]

$$\Gamma_{opt} = 1A_1 + 1E_1 + 2E_2 + 2B_1 \quad (3)$$

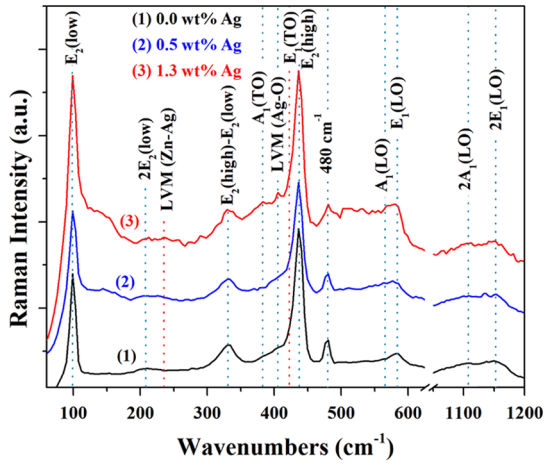

Figure 4. Raman spectra of columnar ZnO:Ag films with different Ag nominal contents.

where A_1, E_1, and E_2 modes are Raman active phonons while A_1 and E_1 are also infrared-active.[41] The A_1 phonon vibrations are polarized parallel to the c axis while the E_1 phonon vibrations are perpendicularly polarized to the c axis.[41]

Figure 4 shows the room temperature Raman spectra of the columnar ZnO:Ag films with Ag nominal content in the spectral range between 60 and 1200 cm^{-1}. For all samples, we observed peaks at around: (i) 99 cm^{-1}, which corresponds to the E_2(low) fundamental phonon mode of ZnO with wurtzite structure and is associated with the heavy Zn sublattice;[42] (ii) 204 cm^{-1}, which corresponds to the $2E_2$(low) second-order phonon mode; (iii) 330 cm^{-1}, which is assigned to the E_2(high)−E_2(low) multiphonon scattering; (iv) 383 cm^{-1}, which corresponds to the A_1(TO) phonon mode; (v) 418 cm^{-1}, which corresponds to the E_1(TO) phonon mode; (vi) 436 cm^{-1}, which corresponds to the E_2(high) phonon mode and involves only the oxygen atoms;[42] (vii) 480 cm^{-1}, which corresponds to the interfacial surface phonon mode; (viii) 567 cm^{-1}, which is assigned to the A_1(LO); (ix) 581 cm^{-1}, which correspond to the E_1(LO) phonon mode that is commonly assigned to the zinc interstitials and oxygen vacancies in ZnO;[42] and (x) 1104 cm^{-1} as well as 1149 cm^{-1}, which correspond to the multiple phonon process of the A_1(LO) and E_1(LO), respectively.[42]

The E_2(low) and E_2(high) phonon modes of the Raman spectra are characteristics of a perfect ZnO crystal, which becomes broader by the addition of Ag.[18] The presence of a Ag dopant also induces an intensity change of A_1(TO) and A_1(LO) polar branches, the E_1(LO) phonon mode, and the broad peak at 144 cm^{-1}, which appears due to lattice vibration.[42] Thus, the Ag incorporation into the columnar ZnO films as well as the TA or RTA treatment at relatively higher temperatures decrease the crystallinity and increase the concentration of the zinc interstitials and oxygen vacancies.[42]

Figure 4 also shows the broadening and intensity changes of the peaks within the range between 500 and 560 cm^{-1} and the A_1(LO) phonon mode for the highly doped sample with 1.30 wt % Ag (curve (3)). This is the consequence of the defects based on silver incorporation as well as Ag segregation at the crystallite interface. The same peaks have been observed previously for Ag-doped ZnO microspheres because of the silver segregation around the grain boundaries and other localized disordered domains[43] and for Mn-doped ZnO nanorods due to the defect-activated mode (M_D) that

DOI: 10.1021/acsami.9b07275
ACS Appl. Mater. Interfaces XXXX, XXX, XXX−XXX

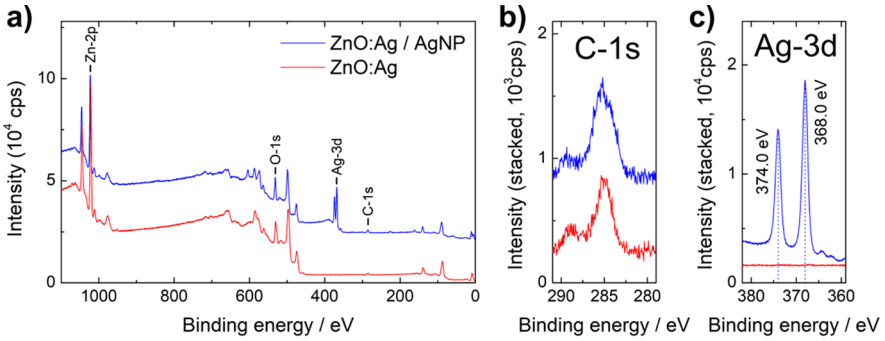

Figure 5. XPS spectra of the ZnO:Ag reference layer (red, bottom line) and the ZnO:Ag nanocomposite decorated with Ag NPs (blue, top line): (a) spectra in the 0−1100 eV region, (b) high-resolution spectra of the C 1s line, and (c) high-resolution spectra of the Ag 3d lines.

represent intrinsic host lattice defects.[44] For both the undoped and Ag-doped columnar ZnO films, we observed an additional mode at 480 cm^{-1} due to an interfacial surface phonon mode.[45] This phonon mode does not depend on the presence or nature of the dopant atom and has also been reported for the Ag-doped ZnO microspheres.[45]

The Raman mapping technique was applied to investigate the spatial distribution of crystallinity and defects in the wurtzite-based ZnO:Ag columnar films containing different Ag concentrations. Figure S4a−d shows the Raman mapping for the E_2 high band integrated between 420 and 450 cm^{-1} for the ZnO:Ag samples and produced using RTA at 575 °C for 60 s. The Raman scattering experiments for both the undoped and doped columnar films show that their crystallinity is relatively uniform, indicating that the doping with Ag atoms does not affect the structural stability of the matrix support. Figure S4e shows the deconvolution using a Gaussian fitting of the 300−460 cm^{-1} Raman spectroscopy range for the sample with 1.3 wt % Ag showing the additional local vibrational modes.

3.4. X-ray Photoemission Spectroscopy (XPS). The X-ray photoemission spectra (XPS) of the Ag/ZnO:Ag nanocomposite (blue line) and the undecorated ZnO:Ag reference thin film (red line) are shown in Figure 5a. The spectra were charge-referenced using the C 1s line of aliphatic carbon, as depicted in Figure 5b. In both the Ag/ZnO:Ag nanocomposite and undecorated ZnO:Ag thin films, we found evidence of C, O, and Zn. The occurrence of C is attributed to atmospheric contamination of the thin film surface, originating from contact with ambient air during handling and transportation of the samples. As expected, no Ag was detected in the undecorated thin film since the dopant concentration is below the detection limit of the XPS instrument. For the Ag NP decorated ZnO:Ag thin film, we observed a well-resolved peak doublet at 368.0 and 374.0 eV, which agrees with the position of the Ag $3d_{5/2}$ and Ag $3d_{3/2}$ lines, respectively (see Figure 5c).[46] Typically, the binding energy of ∼368.2 eV is attributed to metallic Ag, whereas the silver oxides are slightly shifted to lower binding energies of ∼367.9 eV for Ag_2O and 367.6 eV for AgO.[46] Given the small chemical shifts for Ag^+ and Ag^{2+} with regard to metallic Ag, we confirmed the presence of elemental Ag forming the Ag NPs using transmission electron microscopy (TEM).

To investigate the introduction of the Ag dopant, we produced an undecorated ZnO:Ag film with a silver concentration approximately 10-fold the typical value used within this work. For the Ag 3d lines of this thin film, the XPS high-resolution spectrum depicted in Figure S5 was recorded with high pass energy to maximize the signal strength. The observed Ag $3d_{3/2}$ and Ag $3d_{1/2}$ peaks prove the successful incorporation of Ag dopant into the columnar film.[46] We also performed XPS measurements for the Ag/ZnO:Ag sample before and after heat treatment at 350 °C for 1 h (see Figure S6). For the annealed sample, the Ag 3d lines match perfectly the electron binding energy of the same samples, which suggests that the thermal treatment at this temperature and duration has a negligible effect on the oxidation state of the Ag NPs.

3.5. Electrical Properties Characterization. The electrical properties of the ZnO:Ag nanocolumnar films strongly influence the gas sensing behavior toward VOCs.[25] Figure 6a shows the resistivity at 300 K of the columnar Ag-doped ZnO films as a function of the Ag concentration. Note that we treated the samples using different RTA temperatures for 60 s. The electrical resistivity was calculated from the linear

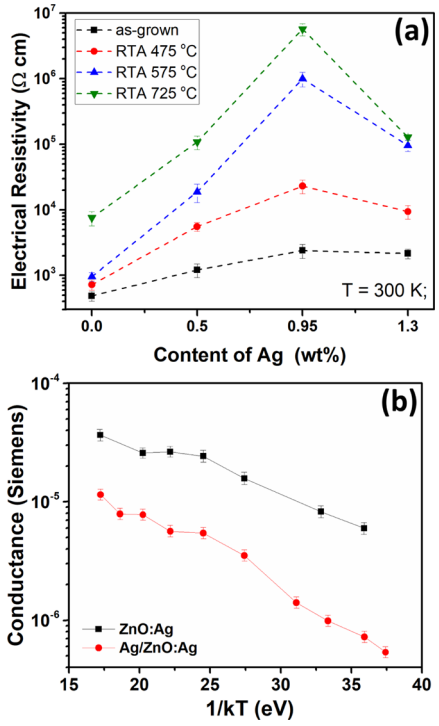

Figure 6. (a) Electrical resistivity of the ZnO:Ag columnar films at 300 K as a function of the Ag nominal content. RTA temperature is indicated. (b) Arrhenius plot for the columnar ZnO:Ag and Ag-functionalized ZnO:Ag (Ag/ZnO:Ag) films with 0.50 wt % Ag and treated using RTA at 725 °C during 60 s.

DOI: 10.1021/acsami.9b07275
ACS Appl. Mater. Interfaces XXXX, XXX, XXX−XXX

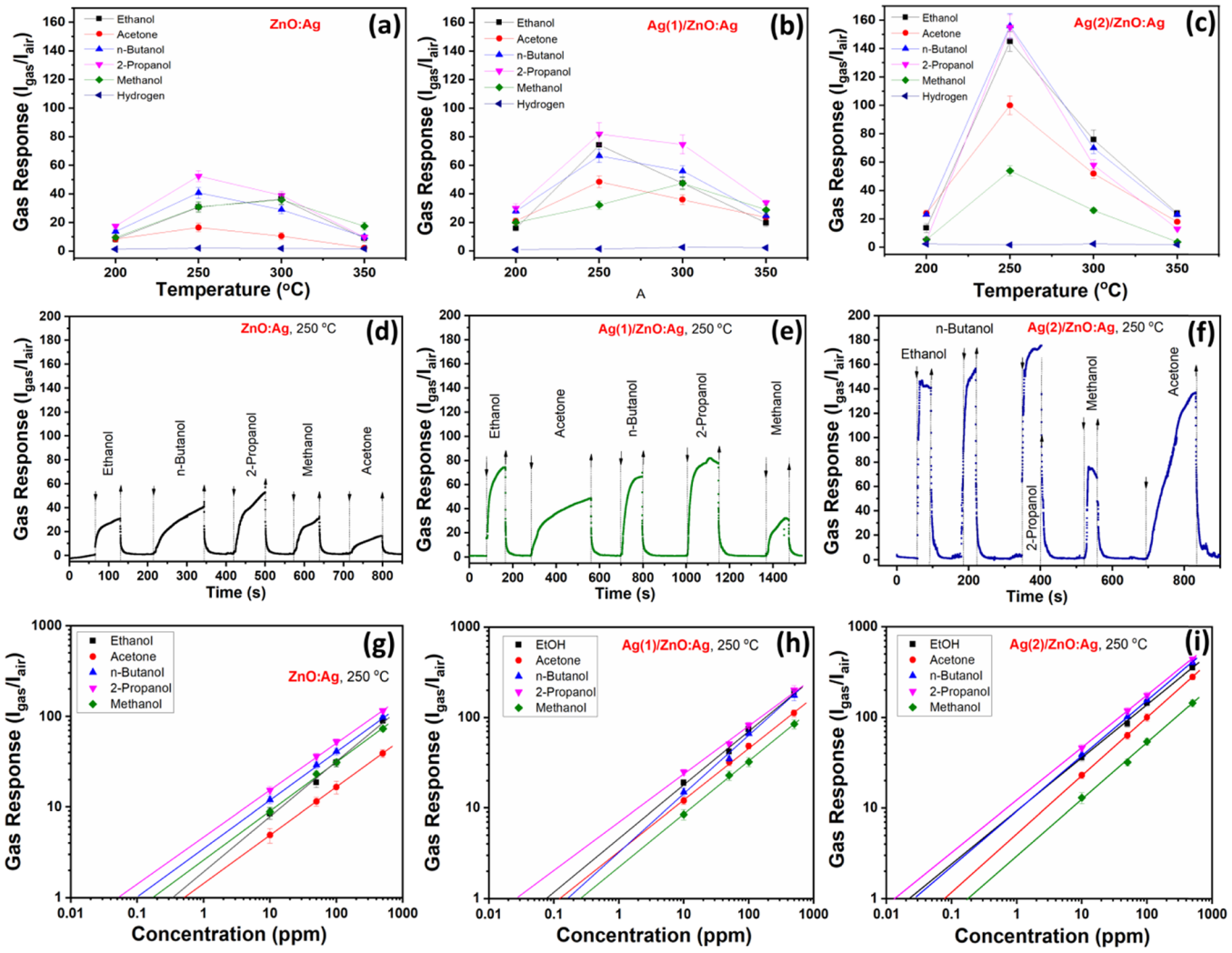

Figure 7. Gas response to 1000 ppm of H_2 gas and 100 ppm of different vapors of volatile organic compounds as a function of the operating temperature for: (a) ZnO:Ag, (b) Ag(1)/ZnO:Ag, and (c) Ag(2)/ZnO:Ag columnar films. Dynamic response to 100 ppm of VOC vapors (at OPT of 250 °C) for: (d) ZnO:Ag, (e) Ag(1)/ZnO:Ag, and (f) Ag(2)/ZnO:Ag columnar film-based sensor structures. The gas response versus concentration of VOC vapors for: (g) ZnO:Ag, (h) Ag(1)/ZnO:Ag, and (i) Ag(2)/ZnO:Ag columnar films.

current−voltage characteristics (meaning ohmic behavior, not shown) of the ZnO:Ag structures enclosed by sputtered Au contact pads using two-wire configuration (see Experimental Section or previous publications).[16−18]

We observed that the electrical resistivities of both ZnO and ZnO:Ag nanocolumnar films increased with the RTA temperature. The elevated RTA temperatures lower the carrier concentration of Zn interstitials, which are lost by evaporation. This finding is supported by previous evidence where postannealing treatments were used to tune the structural, electrical, and optical properties of materials.[46]

The electrical resistivity is also significantly modified by the Ag content in the ZnO:Ag columnar films (see Figure 6a). Silver is an amphoteric dopant of ZnO where it acts as an acceptor on substitutional Zn^{2+} sites (Ag'_{Zn}) or as a donor on the interstitial sites (Ag_i^*).[47] By increasing the silver concentration up to 0.95 wt %, the electrical resistivity of the films sharply increased. At this relatively high concentration, Ag^+ behaves as an acceptor as it prefers to occupy substitutionally the Zn^{2+} sites, as deduced from Raman analyses and supported by XRD (see Figures 2b and 4b). Moreover, positively charged oxygen vacancies ($V_O^{\bullet\bullet}$) that act as acceptors are formed to maintain charge neutrality.[47] By increasing the Ag content further, no reliable p-type behavior was observed in our case. We found that the Ag atoms prefer to occupy the interstitial sites (Ag_i^*) at high concentration of the dopant where they form neutral defects or segregate at the grain boundaries.[47] The large content of electron-rich dopant atoms leads to the reduction in the electrical resistivity of the columnar Ag-doped ZnO films (see Figure 6a).[47] The competition of the Ag^+ ions for the Zn^{2+} or interstitial sites can be rationalized in terms of the relative ionic radii of these ions.[40] It has been suggested that the interstitial holes become the most favorable for the dopant atoms once the substitutional positions are saturated.[47] On the other hand, the reduction in resistivity at Ag contents >0.95 wt % can also be the consequence of the larger grain size detected through the SEM and XRD experiments. The reduced grain boundary density of larger particles results in the weakening of the intergrain boundary scattering and the increase in the carrier lifetime and mobility.[47]

Figure 6b shows the Arrhenius plot of conductance as a function of 1/kT for both the ZnO:Ag and Ag-functionalized ZnO:Ag columnar films with 0.50 wt % Ag obtained using

DOI: 10.1021/acsami.9b07275
ACS Appl. Mater. Interfaces XXXX, XXX, XXX−XXX

Table 1. VOC Sensors Based on Metal Oxides Modified/Decorated with Different Noble Metals

sensing material	VOC conc. (ppm)	gas response (I_{gas}/I_{air}) or (R_{air}/R_{gas})	operating temperature (°C)	response time (s)	recovery time (s)
Ag-ZnO films[64]	ethanol EtOH, 2000	~2	225	5	
Ag-doped ZnO films[39]	ethanol EtOH, 100	~15	260		
Ag-doped ZnO nanorods[65]	ethanol EtOH, 100	19.4	332		
Ag/ZnO nanorods[66]	ethanol EtOH, 100	36.52	360	50	28
ZnO-Ag hybrids[67]	ethanol EtOH, 100	101.8	370	~15	~20
Ag-ZnO nanorods[68]	ethanol EtOH, 50	34.8			
	acetone, 50	25	280		
	methanol, 50	14.5			
Ag-loaded ZnO[69]	ethanol EtOH, 100	~75			
	acetone, 100	~30	240		
	isopropanol, 100	~68			
	methanol, 100	~55			
Ag-doped ZnO-SnO_2 hollow nanofibers[70]	ethanol EtOH, 1	7.6	200	5	5
Ag-(TiO_2/SnO_2)[56]	ethanol EtOH, 50	53	275	3.5	7
ZnO:Ag columnar films (this work)	ethanol EtOH, 100	31			
	acetone, 100	16.5			
	2-propanol, 100	52.5	250		
	n-butanol, 100	41			
	methanol, 100	31			
Ag(2)/ZnO:Ag columnar films(this work)	ethanol EtOH, 100	145 ± 6.2			
	acetone, 100	156 ± 5.8			
	2-propanol, 100		250		
	n-butanol, 100	155 ± 6.5			
	methanol, 100	54 ± 2.1			

RTA at 725 °C during 60 s. For both samples, we observed a double-valued activation energy in which associated conductivity can be expressed as[48]

$$\sigma = \sigma_1 \exp(-E_{a1}/kT) + \sigma_2 \exp(-E_{a2}/kT) \quad (4)$$

where E_{a1} is the activation energy for the band conduction, E_{a2} is the activation energy for the nearest neighbor hopping conduction, k is the Boltzmann constant, σ_1 and σ_2 are the preexponential factors, and T is the absolute temperature.[48] The E_{a1} values of 52.9 and 78.6 meV were obtained for ZnO:Ag and Ag/ZnO:Ag, respectively, which are consistent with other results on ZnO films.[48,49] The E_{a2} values of 24.4 and 44.8 meV were obtained for ZnO:Ag and Ag/ZnO:Ag thin films, respectively, which are widely assigned to the thermionic emission over grain boundaries.[48,49] Figure 6b also depicts the reduction in the conductance of ZnO:Ag films after functionalization with Ag nanoparticles due to enhanced oxygen adsorption, which traps conduction electrons.[48,49]

3.6. Gas Sensing Properties of Ag(1)/ZnO:Ag and Ag(2)/ZnO:Ag Columnar Films. Figure 7a–c shows the gas response of the ZnO:Ag, Ag(1)/ZnO:Ag, and Ag(2)/ZnO:Ag columnar films to 1000 ppm of H_2 gas and 100 ppm of VOC vapors (ethanol, acetone, *n*-butanol, 2-propanol, and methanol), respectively. As the carrier gas, the ambient air with ~30% relative humidity (RH) was used. Measurements in the temperature range between 200 and 350 °C were performed. For all samples, no considerable H_2 response, even with using the highest concentration of 1000 ppm, was observed. The optimal operating temperature for the columnar ZnO:Ag films is 250 °C (see Figure 7a), where the gas responses to 100 ppm of ethanol, acetone, *n*-butanol, 2-propanol, and methanol are ~31, ~16.5, ~41, ~52.5, and ~31, respectively. After functionalization with Ag NPs, the optimal operating temperature remained at 250 °C (see Figure 7b,c), and the gas responses to 100 ppm of ethanol, acetone, *n*-butanol, 2-propanol, and methanol are ~74, ~48.5, ~67, ~82, and ~32 for Ag(1)/ZnO:Ag and ~145, ~100, ~156, ~175, and ~54 for Ag(2)/ZnO:Ag, respectively. The gas response increased by adding Ag NPs, which are known to weaken the adsorption and desorption of adsorbates on metal oxides and accelerate their reaction with oxygen.[50] Our results for the columnar ZnO:Ag and Ag-functionalized ZnO:Ag films are highly improved compared to reports for the undoped and Ag-modified ZnO micro and columnar films[18] (see Table 1). The possible mechanism for such improved performances is discussed in Section 3.7.

Figure 7d–f and Figure S7 show the dynamic response of pristine and Ag-functionalized ZnO:Ag columnar films, respectively, to 100 ppm of VOC vapors at different operating temperatures. We observed that all samples show fast response recoveries after evacuation of the VOC vapor from the test chamber. The calculated response and recovery times decrease with the operating temperatures are presented in Figure S8a for ZnO:Ag, Figure S8b for Ag(1)/ZnO:Ag, and Figure S8c for Ag(2)/ZnO:A. The calculated gas sensing parameters including the response value as well as the response and recovery times are summarized in Table S1 for ZnO:Ag, Ag(1)/ZnO:Ag, and Ag(2)/ZnO:Ag columnar films.

The dependence of gas response (S) versus concentration of VOC vapors (p_{VOC}) for ZnO:Ag, Ag(1)/ZnO:Ag, and Ag(2)/ZnO:Ag columnar films is presented in Figure 7g–i, respectively. All samples showed a power law relationship to the varied VOC concentrations (from 10 to 500 ppm), $S \propto p_{VOC}^{\beta}$, where β is the slope of log S versus log p_{VOC}.[27] For all samples, β varies from 0.5 to 0.67. The theoretical detection limits (DL) were estimated from Figure 7g–i, as was reported by Dua et al.[51] The estimated values of DL for ethanol, acetone, *n*-butanol, 2-propanol, and methanol are 0.48, 0.66,

DOI: 10.1021/acsami.9b07275
ACS Appl. Mater. Interfaces XXXX, XXX, XXX−XXX

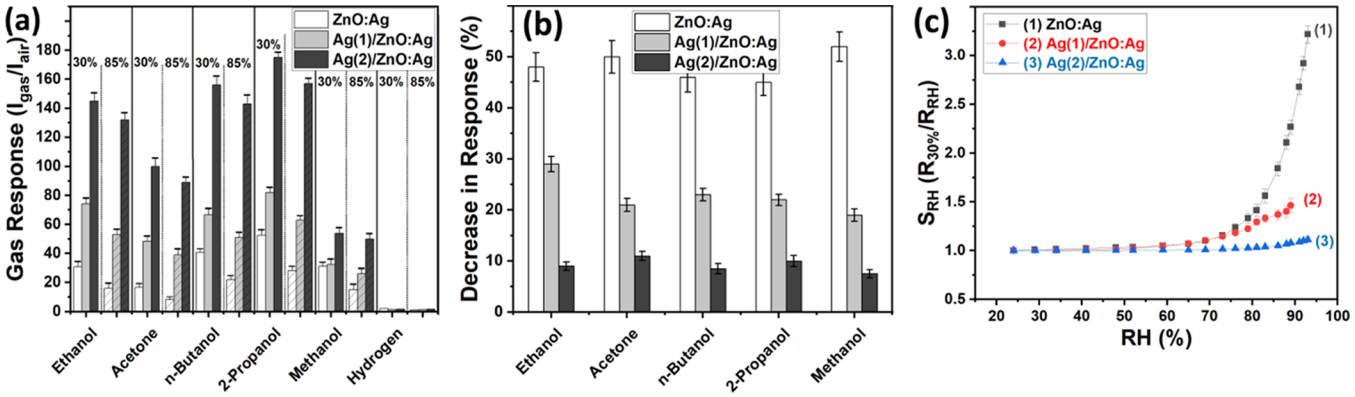

Figure 8. (a) Calculated gas response at 250 °C operating temperature for ZnO:Ag, Ag(1)/ZnO:Ag, and Ag(2)/ZnO:Ag columnar films to 100 ppm of VOC vapors and 1000 ppm of H_2 gas under different relative humidity conditions (30 and 85%). (b) Calculated decrease in response at 250 °C operating temperature to 100 ppm of VOC vapors by increasing the RH from 30 to 85%. (c) Room temperature response of ZnO:Ag, Ag(1)/ZnO:Ag, and Ag(2)/ZnO:Ag versus relative humidity.

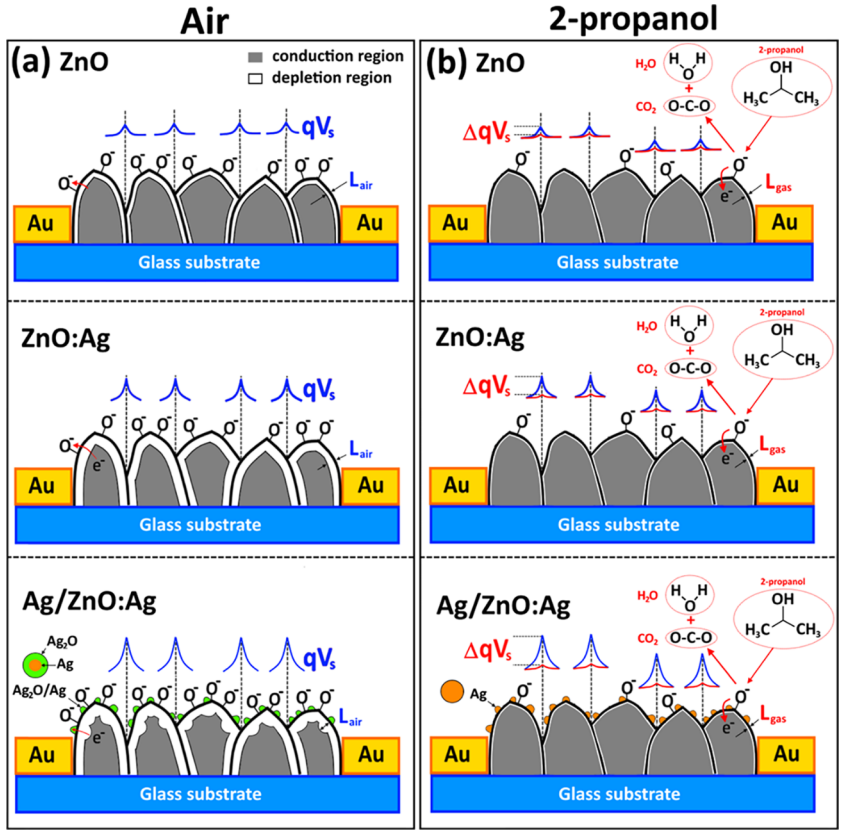

Figure 9. Proposed gas sensing mechanism for ZnO, ZnO:Ag, and Ag/ZnO:Ag columnar films integrated in sensor structures during exposure to: (a) ambient air and (b) 2-propanol vapors.

0.22, 0.13, and 0.06 ppm for ZnO:Ag, 0.1, 0.17, 0.21, 0.05, and 0.37 ppm for Ag(1)/ZnO:Ag, and 0.02, 0.07, 0.04, 0.01, and 0.24 ppm for Ag(2)/ZnO:Ag columnar films, respectively. Therefore, by functionalization with higher density of Ag NPs, we can effectively decrease the detection limit of our columnar films, which for ethanol is in excellent agreement with the value of 10 ppb found for NiO−ZnO p−n nanoheterojunction networks.[52] The gas response and DL of samples are summarized in Table S2.

Variation in the atmospheric humidity levels is an important factor that determines the sensing properties of gas sensors based on the metal oxide micro and nanostructures due to the hydroxyl poisoning.[6,7] Therefore, we performed the gas sensing measurements at a low RH value of ∼30% and high RH value of ∼85%, respectively. The higher value of RH was generated using a bubbling system.[27]

Figure 8a shows the gas response to 100 ppm of VOC vapors and 1000 ppm of H_2 gas for ZnO:Ag, Ag(1)/ZnO:Ag, and Ag(2)/ZnO:Ag samples at an optimal operating temperature of 250 °C under different conditions of relative humidity (RH), that is, at a lower value of 30% and a higher value of 85%. The decrease in response for all samples by the increase in RH was observed (see Table S3). In the case of the ZnO:Ag columnar film, by increasing RH from 30 to 85%, the decreases

DOI: 10.1021/acsami.9b07275
ACS Appl. Mater. Interfaces XXXX, XXX, XXX−XXX

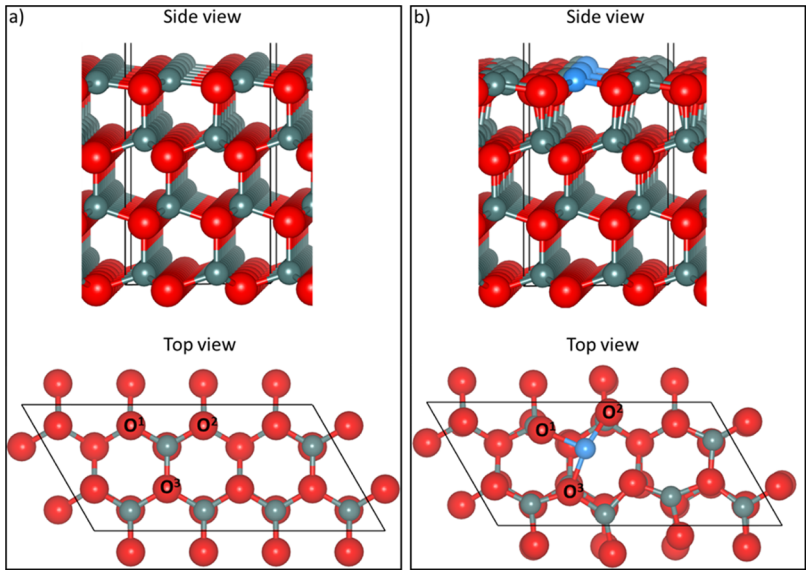

Figure 10. (Top panel) side and (bottom panel) top views of the (a) relaxed ZnO(0001) pristine surface and (b) Ag-doped ZnO(0001) surface. Color key: red, green, and blue represent O, Zn, and Ag atoms, respectively.

in response for 100 ppm of ethanol, acetone, *n*-butanol, 2-propanol, and methanol are ~48, ~50, ~46, ~45, and ~52%, respectively. After functionalization with Ag NPs, the lower decrease in response by increasing RH was observed. The decreases in response for 100 ppm of ethanol, acetone, *n*-butanol, 2-propanol, and methanol is ~29, ~21, ~23, ~22, and ~19%, respectively, for Ag(1)/ZnO:Ag and ~9, ~11, ~8.5, ~10, and ~7.5%, respectively, for Ag(2)/ZnO:Ag. Therefore, it is demonstrated that by surface functionalization of ZnO:Ag columnar films with Ag NPs, an improvement in stability under humidity changes can be achieved (see Figure 8b). These results may indicate that Ag NPs act as hydroxyl absorbers, which was also observed, for example, for Sb atoms[6] and CuO.[53] Ag NPs were found to be excellent humidity sensors with excellent stability.[54,55] This can also explain the lower decrease in response by higher density of Ag NPs.

To experimentally demonstrate the lower dependence of resistance for Ag NP-functionalized ZnO:Ag columnar films on RH, the room temperature measurements of resistance versus RH were performed, and the results are presented in Figure 8c. The RH response (S_{RH}) was defined as the ratio of the resistance under 30% RH ($R_{30\%}$) and under the measured RH value (R_{RH}). The larger change in resistance by increasing RH for samples without Ag NPs was observed, while by increasing the density of Ag NPs, the dependence of resistance on RH is lowered. These results reveal the excellent potential of Ag NP-functionalized ZnO:Ag columnar films for real-time environmental monitoring.

3.7. Proposed Gas Sensing Mechanism for Columnar Films. The gas sensing mechanism of the undoped ZnO columnar films was already discussed in our previous work.[18] We explained the gas sensing mechanism based on the modulation of potential barriers ($q\Delta V_S$) between the ZnO grains due to adsorption/desorption of oxygen species, which modulates the surface electron depletion region.[18] We also discussed the role of the interconnection−interpenetration of the ZnO grains, enhancing the modulation of $q\Delta V_S$, which governs the gas response (S)[18]

$$S = \frac{R_{air}}{R_{gas}} \approx \exp\left(-\frac{q\Delta V_S}{2kT}\right) \quad (5)$$

where R_{air} and R_{gas} are the resistance in air and under gas exposure, respectively, and q is the electrical charge of the carrier.

As we have already discussed in this work, doping with Ag generates more acceptors in ZnO, which decrease the charge-carrier concentration (n) and enlarge the electron depletion region (L)[12,18]

$$L = (2\varepsilon_{ZnO}\varepsilon_0 V_S/qn)^{1/2} \quad (6)$$

where ε_{ZnO} is the dielectric constant of ZnO and V_S is the interfacial potential.[12,18] Under air exposure, oxygen adsorb onto the surface of grains, which increases the length of L_{air} for the Ag-doped samples, compared to the undoped ZnO (see Figure 9a)[12,18]

$$O_2(g) \rightarrow O_2(ad) \quad (7)$$

$$\frac{1}{2}O_2(ad) + e^- \rightarrow O^-(ad) \quad (8)$$

For the Ag-functionalized samples, the L_{air} value due to enhanced adsorption of oxygen species further increased. The excellent catalytic properties of Ag as dopant and NPs lead to increasing the length of the electron depletion region, L_{air} (ZnO) < L_{air} (ZnO:Ag) < L_{air} (Ag/ZnO:Ag) (see Figure 9a). Our results clearly show that Ag NP functionalization of the ZnO:Ag grains facilitates faster adsorption and desorption of the oxygen species as well as quicker capture of free electrons.[56] We also found evidence that the surfaces of the Ag NPs are easily oxidized to Ag_2O in air at the relatively low operating temperature of 250 °C.[14,56] We can justify the reactivity of the Ag NPs toward oxygen due to their large Helmholtz double layer,[56] which allow them to act as efficient electron sinks. The oxygen adsorption on the surfaces of Ag_2O leads to the electron extraction from ZnO:Ag effectively extending the width of electron depletion region to the supporting grain (see Figure 9a).[14,56] Given the direct relationship between L and V_S, we found the same increasing

DOI: 10.1021/acsami.9b07275
ACS Appl. Mater. Interfaces XXXX, XXX, XXX−XXX

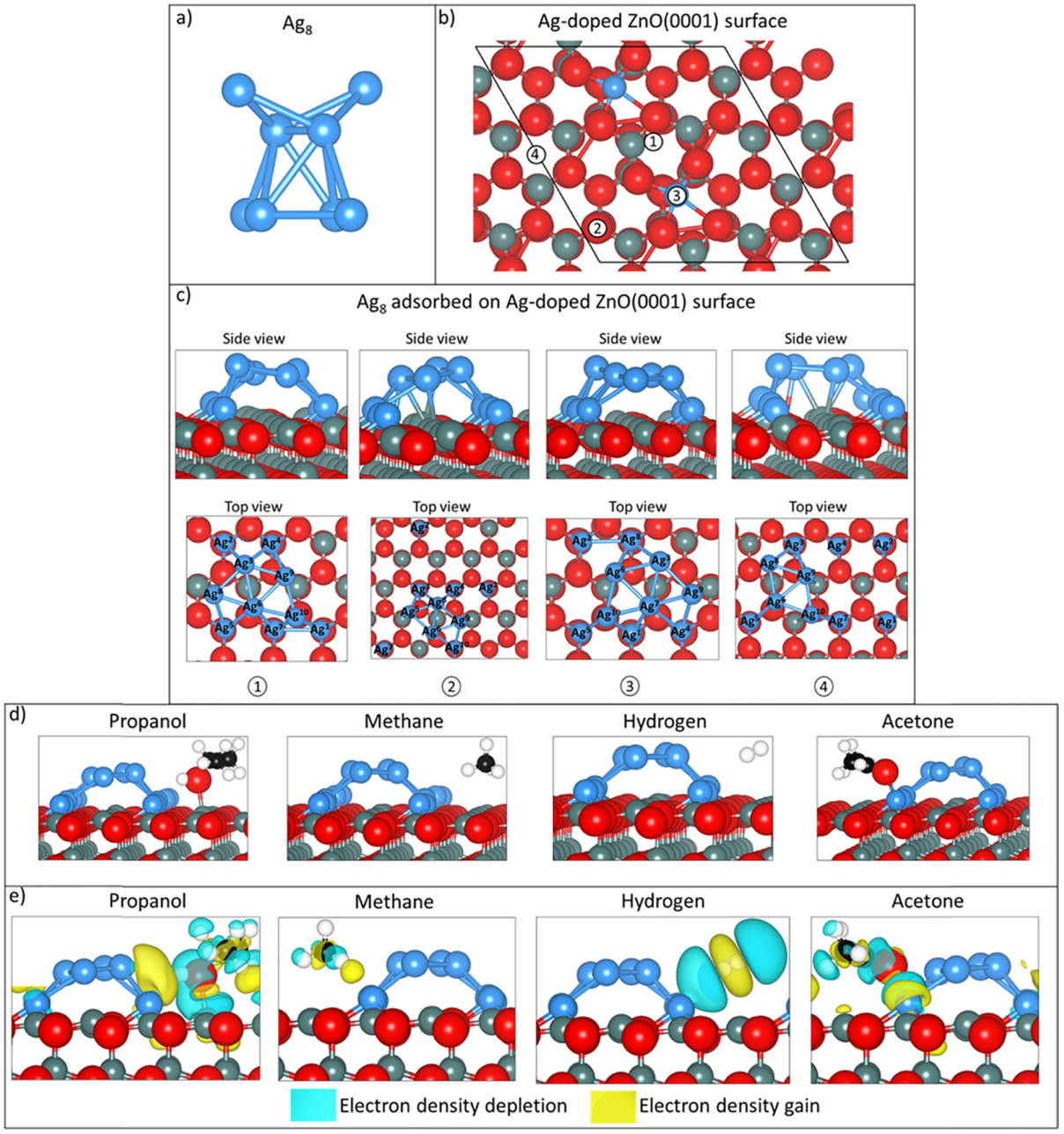

Figure 11. (a) Initial Ag_8 cluster geometry. (b) Initial adsorption sites for the Ag_8 center of mass: (1) between two dopant atoms, (2) near the dopant, (3) above the dopant, (4) and far away from the dopant. (c) Final adsorption geometries. (d) Most stable geometries and (e) electron density difference of propanol, methane, hydrogen, and acetone adsorbed on the Ag_8/ZnO(0001) surface doped with Ag. Color key: red, green, blue, black, and white represent O, Zn, Ag, C, and H atoms, respectively.

order for the potential barrier height (qV_S), that is, qV_S (ZnO) < qV_S (ZnO:Ag) < qV_S (Ag/ZnO:Ag) (see Figure 9a).

We now focus on the detection of 2-propanol vapors ($(CH_3)_2CHOH$) due to the slightly higher response compared to the other VOC gases. The gas sensing mechanism is similar for all VOC vapors, apart from the different reactions with oxygen species coadsorbed on the grain surfaces.[57] The higher response to 2-propanol vapors compared to other VOC gases (see Figure 9b) can be explained based on the quantity of electrons released during the decomposition and oxidation, according to the reaction.[57]

$$(CH_3)_2CH - OH + 9O^- \rightarrow 3CO_2 + 4H_2O + 9e^- \quad (9)$$

Our results show that for the most effective Ag/ZnO:Ag sensor, the narrow electron depletion region (L_{gas}) leads to the reduction of the potential barriers height (qV_S) (see Figure 9b). According to eq 6, the highest modulation and gas response are reached using the Ag/ZnO:Ag samples, followed by ZnO:Ag and then by ZnO. For the Ag/ZnO:Ag samples, the Ag_2O formed spontaneously on the surface of the NPs is reduced back to Ag under exposure to VOC vapors, providing electrons to ZnO[14] and leading to an enhanced gas response. Thus, reported results support claims that hybrid Me_xO_y and $Zn_xMe_{1-x}O_y$ alloyed ZnO networks are very important for sensing applications.[37,67,71]

3.8. Density Functional Theory Simulations. *3.8.1. Pristine ZnO(0001) Surface.* Computational details on DFT

DOI: 10.1021/acsami.9b07275
ACS Appl. Mater. Interfaces XXXX, XXX, XXX−XXX

simulations are presented in the Supporting Information. Figure 10a shows the relaxed, clean ZnO(0001) surface where we observed an inward displacement of the Zn atoms belonging to the topmost layer during relaxation. The consequence of the displacements is the contraction of the Zn−O bonds in the top two atomic layers. Before relaxation, the average Zn−O distance is 1.947 Å, while after relaxation, this value drops to 1.860 Å. For the rest of the atoms in the surface slabs that were allowed to relax, we observed a negligible displacement.

3.8.2. Doped ZnO(0001) Surface. We next doped the ZnO(0001) surface with Ag. In the Experimental Section, the maximum Ag content considered is 1.3 wt %. As our oxide surface cell contains 60 atoms, we replaced one Zn to obtain 1.7 wt % of Ag, which is close to the experimental doping concentration. Following our previous investigation[20] where we showed that a metallic dopant prefers to occupy the most exposed surface site, we positioned the silver atom at the top layer (see Figure 10b). We found that the Ag atom moves away from its neighboring O atoms (O^1, O^2, and O^3 in Figure 10b) during optimization due to the larger ionic radii of Ag compared to Zn (see Experimental Section). This movement is observed mainly in the surface layer, as the average in-plane displacement of the silver atom is 0.220 Å while the outward shift is 0.099 Å. Our simulations suggest that the Zn−O bond distance around the Ag dopant undergoes an average decrease of 0.016 Å following the creation of the defect. We note that similarly to Ag, both O and Zn atoms move mainly in the direction of the surface plane.

The Bader charge analysis of O^1 and O^2 reveals that these atoms, which are equally charged, are oxidized by 0.1 e^- after doping. Thus, the charge transfer from Ag to the neighboring O is less important than the one from Zn to O.

We next describe the Zn−O and Ag−O interaction by plotting the electronic density of states (DOS) of both the pristine and Ag-doped Zn(0001) surfaces (see Figure S9a,b). The calculated band gap of the pristine surface is 0.74 eV, which is in excellent agreement with the theoretical value of 0.75 eV reported by Mohamad et al.[58] We also note from Figure S9a,b that for both surfaces, the contribution to the valence band comes mainly from the O 2p orbitals. The Zn 3d orbitals are dominant at lower energies, approximately between −8.00 and −6.00 eV and are thus expected to have less influence in the surface properties of the material than the O atoms.

We plotted the projected DOS of the O^1 and O^2 p orbitals and the *d* states of the metal atom bonded to them for both the pristine and Ag-doped Zn(0001) surfaces (see Figure S9c,d). In the pristine surface, as shown in Figure S9c, we note that just below the Fermi level, the Zn 3d and O^1 and O^2 2p orbitals are located at the same energy, at −0.19 and −0.61 eV. The hybridization between those electronic states suggests a significant interaction between the atoms. From the DOS of the doped surface shown in Figure S9d, we note that just below the Fermi level, the intensities of the Ag 4d orbitals and the neighboring oxygen 2p orbitals are higher than the one found in the pristine surface. This suggests that in the doped surface, the Ag−O interaction is stronger than Zn−O in the clean surface. Thus, the Ag−O interaction is less ionic, that is, more covalent, than the Zn−O interaction, which is further supported by the smaller charge transfer from Ag to O than from Zn to O.

3.8.3. Cluster Adsorption. We next evaluated the adsorption of the Ag_8 cluster onto the Ag-doped ZnO(0001) surface (see Figure 11a). We tried four adsorption sites: between, close, on top, and away from the Ag dopant atoms (see Figure 11b). The initial Ag_8 structure, prior to geometry optimization, was similar to the one employed by Idrobo et al.[59] where they determined the ground state of [isolated] Ag_n (n = 2−8) clusters. Thus, as shown in Figure 11a, we adopted a 3D shape where the average distance between the silver atoms is 2.72 Å. For all the configurations, we positioned the Ag_8 cluster approximately 2 Å above the oxide surface.

The optimized geometry of the initial adsorption site 1 shows that Ag_8 tends to disaggregate as some of the Ag atoms leave the cluster to adsorb on the surface (see Figure 11c). Interestingly, we found that the cluster atoms filled the Zn vacancies that were created to quench the dipole moment (see the Computational Details Section). Figure 11c shows that Ag^4, similarly to the Ag dopant, sits in the center of mass of the triangle formed by three oxygens. The adsorption site of Ag^4 is similar to the highly symmetric site described by Lloyd et al.[60] where they used lattice-based adaptive kinetic Monte Carlo (LatAKMC) to describe Ag adsorption on top of the polar ZnO(0001) surface. The average distance between Ag^4 and its neighboring oxygens is 2.442 Å, which is close to the average dopant−surface oxygen distance of 2.208 Å. The same observation can be made for Ag^5 and Ag^7, which are located in the center of masses of the neighboring oxygen atoms at average distances of 2.303 and 2.263 Å, respectively.

Similarly, for the adsorption site number 3, three Ag atoms leave the cluster to adsorb on the surface. The average distance between the detached Ag^4, Ag^5, and Ag^8 and their neighboring oxygen atoms is 2.302, 2.259, and 2.279 Å, respectively.

In both adsorption sites 2 and 4, four Ag atoms leave the cluster to adsorb on the surface. Figure 11c shows that for both configurations, the leaving atoms (Ag^3, Ag^4, Ag^7, and Ag^{10} for configuration 2 and Ag^3, Ag^4, Ag^5, and Ag^7 for configuration 4) adsorb on the surface at average distances from their neighboring oxygen atoms between 2.244 and 2.304 Å, respectively. For the four adsorption configurations, the average distance between the remaining aggregated Ag atoms is ∼2.8 Å, with geometries similar to the clusters described by Idrobo et al.[59] From the geometry analysis, we note that surrounding an adsorbed Ag_8 cluster with Ag dopants would maintain the aggregated geometry of the cluster, favoring the Stranski−Krastanov growth that has been observed experimentally[61] and theoretically.[60,62]

We next calculated the clustering energy and found that the most stable structures are for configurations 2 and 4 (0.31 and 0.32 eV, respectively), while configurations 1 and 3 are slightly less stable (0.36 and 0.38 eV, respectively). These energy values suggest that the adsorption is stronger for the clusters placed away from the dopant. The positive clustering energies show that the clusters tend to aggregate rather than completely wet the surface, although their small values indicate a competition between these two processes.

We also calculated the average Bader charge of the cluster and found average charges of +0.2, +0.3, +0.2, and + 0.3 e^- for configurations 1, 2, 3, and 4, respectively. The charges are in line with the clustering energies as most positive clusters, that is, where we observe the strongest charge transfer to the surface, are found for the most stable configurations 2 and 4. From the Bader analysis, we also observed a charge reorganization for all the configurations where some Ag

DOI: 10.1021/acsami.9b07275
ACS Appl. Mater. Interfaces XXXX, XXX, XXX−XXX

atoms that are not directly bonded to the surface have a negative charge. This charge segregation within the Ag cluster has been observed previously by Hirunsit et al.[63] in Ag_{13} clusters adsorbed on Al_2O_3.

3.8.4. Molecules Adsorption. We chose the most stable configuration, that is, configuration 2 (see Figure 11c), to study the interaction between Ag_8/ZnO(0001) doped with Ag and propanol (C_3H_8O), methane (CH_4), hydrogen (H_2), and acetone ($(CH_3)_2CO$). For each molecule, we considered several orientations and adsorption sites: at the interface between the Ag_8 cluster and the ZnO surface, above the cluster, and far away from the cluster. However, we describe here only the most stable geometry.

Propanol adsorbs molecularly on the surface, and the most favorable adsorption site is far away from the cluster (see Figure 11d). The calculated binding energy is −1.00 eV, and the molecule surface distance is 2.214 Å.

Propanol interacts with the surface through its hydroxyl termination, which becomes slightly weaker after adsorption as the O−H distance increases by 0.020 Å. We also note a slight increase by 0.01 Å of the C−H bond distance for hydrogen facing the surface. The OH−surface interaction is confirmed by the electron density difference plot where we observe a slight charge gain between the hydrogens facing the surface and the surface (see Figure 11e). However, the large charge accumulation (depletion) between the OH termination and the Ag_8 cluster (Zn surface atoms) further supports that the polar group is the main interaction center. We calculated the Bader charge of the Zn atom interacting with the propanol OH group and noted that the positive charge increases slightly from +1.1 to +1.2 e^- after adsorption.

Acetone also adsorbs molecularly with a binding energy of −0.88 eV and prefers to interact with the doped ZnO(0001) surface through the carbonyl oxygen atom. Figure 11d shows the interaction between the acetone/oxygen and two Ag atoms adsorbed on the surface at 2.529 Å. Concerning the intramolecular bonds, the C═O distance increases by 0.020 Å, suggesting a weakening due to the interaction with the surface. The other internal distances are barely affected by the surface as we only observe a small contraction of 0.01 Å of both C−C bonds. The electron density difference shown in Figure 11e confirms the interaction between the acetone oxygen and the silver atoms as both depletion and gain occur between them. However, this is a charge rearrangement rather than a transfer as the Bader charge of the silver atoms involved in the interaction is unchanged after the molecule adsorption. Thus, the energetic, structural, and electronic analyses confirm that the acetone−surface interaction is weaker than the propanol−surface interaction.

Figure 11d shows that both methane and hydrogen prefer to adsorb away from the cluster, interacting weakly with the surface as the calculated binding energies are −0.29 and −0.11 eV, respectively. The distance analysis also confirms the weak adsorption: CH_4 is positioned at 2.904 Å from the surface while H_2 is 3.123 Å above the surface. Those distances are larger than the ones found for acetone and propanol. Additionally, the molecular internal distances are not affected by the adsorption, showing that the molecule−surface interaction is not strong enough. The electron density difference shows that only a polarization of the molecule orbitals takes place (see Figure 11e). The Bader charge analysis also proves that CH_4 and H_2 are physisorbed on the surface as all atomic charges remain unchanged after the adsorption. Our computational results suggest that the interaction is stronger for molecules containing oxygen atoms, which can coordinate the surface Zn or cluster Ag atoms.

4. CONCLUSIONS

In summary, we developed a novel strategy to modulate the density of Ag nanoparticles uniformly on nonplanar ZnO:Ag columnar films by a one-step sputtering method followed by thermal annealing at 350 °C. By elucidating the concerning mechanisms, we demonstrated the synergistic role of doping and surface functionalization using Ag nanoparticles in enhancing the gas sensing response and selectivity of semiconducting oxides, namely, ZnO, toward specific volatile organic compounds. These results are important for the use of new hybrid sensing nanomaterials, which enable simpler differentiation between various VOCs. The latter can serve as biomarkers for diseases at early stages since VOCs detected in exhaled breath at the ppb level are related to several diseases.

The gas sensing properties of such hybrid materials showed that the Ag-functionalized ZnO:Ag samples offer significantly improved VOC sensing properties in an operating temperature range of 150−200 °C. The Ag-doped and Ag NP-functionalized ZnO:Ag columnar films were successfully synthesized as a single crystalline columnar matrix via a cost-effective SCS method, which allows for deposition on almost any material. The computational simulations showed that a few Ag atoms disaggregate from the cluster, which prefers to sit far away from the dopant. The gas sensing properties toward ethanol, acetone, *n*-butanol, 2-propanol, and methanol vapors improved after doping the ZnO columnar films with Ag. Further enhancement of the sensing properties of the Ag-doped ZnO columnar films toward VOC vapors by surface functionalization with Ag NPs of diameters between 6 and 12 nm was obtained experimentally, which is in agreement with the computational simulations. The synergistic effect of the Ag dopant atoms and Ag clusters on the ZnO columnar films is found to be highly beneficial for the response toward the detection of VOC gases. Experimental and theoretical evidence confirmed the importance of both approaches, doping and surface functionalization at the same time, for advancing the nanotechnology and nanoscience of new functional materials. Our work shows that highly selective and sensitive sensors used to distinguish specific VOC molecules are essential not only for air quality monitoring and various industrial applications but also for a simple manner to detect biomarkers for early stage diseases.

■ ASSOCIATED CONTENT

Supporting Information

The Supporting Information is available free of charge on the ACS Publications website at DOI: 10.1021/acsami.9b07275.

SEM image of ZnO:Ag and Ag/ZnO:Ag columnar films at different magnifications; column size histogram of ZnO:Ag columnar films with different contents of Ag; Raman mapping for the E_2(high) band (integrated between 420 and 450 cm^{-1}) of the ZnO:Ag columnar films and the deconvolution of the 300−460 cm^{-1} region using a Gaussian fit; XPS plot of the Ag 3d lines of ZnO:Ag with increased (10-fold) Ag doping concentration; dynamic response to 100 ppm of VOC vapors for ZnO:Ag and Ag/ZnO:Ag at different

DOI: 10.1021/acsami.9b07275
ACS Appl. Mater. Interfaces XXXX, XXX, XXX−XXX

operating temperatures; response and recovery times as a function of temperature for ZnO:Ag and Ag/ZnO:Ag; electronic density of states (DOS) of the pristine and Ag-doped ZnO(0001) surfaces and atomic projected DOS of the pristine and Ag-doped ZnO(0001) surfaces (PDF)

AUTHOR INFORMATION

Corresponding Authors

*E-mail: SantosCarballalD@cardiff.ac.uk (D.S.-C.).
*E-mail: deLeeuwN@cardiff.ac.uk (N.H.d.L.).
*E-mail: ra@tf.uni-kiel.de (R.A.).
*E-mail: ff@tf.uni-kiel.de (F.F.).
*E-mail: ollu@tf.uni-kiel.de; oleg.lupan@mib.utm.md; lupan@physics.ucf.edu (O.L.).

ORCID

Franz Faupel: 0000-0003-3367-1655

Author Contributions

O.L., V.P., and A.V. synthesized the Ag-functionalized ZnO:Ag material. O.L. developed synthesis from chemical solution procedure SCS for ZnO. O.L., V.P., A.V., M.-I.T., and M.H. adapted the technological approach for material synthesis and integration/fabrication of the sensors. A.V. and F.F. developed Ag functionalization procedure and setup and realized all experiments and XPS analysis. P.V. and O.L. carried out the measurement of sensing properties of sensors based on such structures and analyzed data. T.D. and L.K. studied TEM. V.P., O.L., M.H., R.A., and M.-I.T. analyzed the results, including Raman data and revised draft. N.H.d.L., D.S.-C., and A.C.-E. realized the computational part. A.V., P.V., A.C.-E., D.S.-C., R.A, and O.L. drafted the article. O.L., F.F., N.H.d.L., L.K., and R.A. conceived and designed the study and approved the final version of the manuscript to be published. All authors reviewed the manuscript.

Notes

The authors declare no competing financial interest.

ACKNOWLEDGMENTS

Dr. Lupan acknowledges the Alexander von Humboldt Foundation for the research fellowship for experienced researchers 3-3MOL/1148833 STP at the Institute for Materials Science, Kiel University, Germany. The German Research Foundation (DFG) sponsored partially this research through the research unit FOR2093. This research was partly supported by the STCU and ASM within the Grant 6229A and by the Technical University of Moldova. We acknowledge the Engineering and Physical Sciences Research Council (EPSRC grant EP/K009567) for funding. Through our membership of the UK's HEC Materials Chemistry Consortium, which is funded by EPSRC (EP/L000202), this work used the ARCHER UK National Supercomputing Service (http://www.archer.ac.uk). This work was performed using the computational facilities of the Advanced Research Computing at Cardiff (ARCCA) Division, Cardiff University. The authors also acknowledge the use of HPC Wales, Supercomputing Wales, and associated support services in the completion of this work. All data created during this research is openly available from the Cardiff University's Research Portal at http://doi.org/10.17035/d.2019.0081497456.

REFERENCES

(1) Righettoni, M.; Amann, A.; Pratsinis, S. E. Breath analysis by nanostructured metal oxides as chemo-resistive gas sensors. *Mater. Today* **2015**, *18*, 163−171.
(2) Wang, Z. L.; Song, J. Piezoelectric Nanogenerators Based on Zinc Oxide Nanowire Arrays. *Science* **2006**, *312*, 242.
(3) Hu, X.; Masuda, Y.; Ohji, T.; Kato, K. Micropatterning of ZnO Nanoarrays by Forced Hydrolysis of Anhydrous Zinc Acetate. *Langmuir* **2008**, *24*, 7614−7617.
(4) Hu, X.; Masuda, Y.; Ohji, T.; Kato, K. Fabrication of Blanket-Like Assembled ZnO Nanowhiskers Using an Aqueous Solution. *J. Am. Ceram. Soc.* **2009**, *92*, 922−926.
(5) Hu, X.; Shen, X.; Huang, R.; Masuda, Y.; Ohji, T.; Kato, K. A facile template-free route to synthesize porous ZnO nanosheets with high surface area. *J. Alloys Compd.* **2013**, *580*, 373−376.
(6) Suematsu, K.; Sasaki, M.; Ma, N.; Yuasa, M.; Shimanoe, K. Antimony-Doped Tin Dioxide Gas Sensors Exhibiting High Stability in the Sensitivity to Humidity Changes. *ACS Sens.* **2016**, *1*, 913−920.
(7) Bai, Z.; Xie, C.; Hu, M.; Zhang, S.; Zeng, D. Effect of Humidity on the Gas Sensing Property of the Tetrapod-Shaped ZnO Nanopowder Sensor. *Mater. Sci. Eng. B* **2008**, *149*, 12−17.
(8) Lupan, O.; Postica, V.; Labat, F.; Ciofini, I.; Pauporté, T.; Adelung, R. Ultra-Sensitive and Selective Hydrogen Nanosensor With Fast Response at Room Temperature Based on a Single Pd/ZnO Nanowire. *Sens. Actuators, B* **2018**, *254*, 1259−1270.
(9) Gröttrup, J.; Postica, V.; Ababii, N.; Lupan, O.; Zamponi, C.; Meyners, D.; Mishra, Y. K.; Sontea, V.; Tiginyanu, I.; Adelung, R. Size-Dependent UV and Gas Sensing Response of Individual Fe_2O_3-ZnO:Fe Micro- and Nanowire Based Devices. *J. Alloys Compd.* **2017**, *701*, 920−925.
(10) Lupan, O.; Postica, V.; Gröttrup, J.; Mishra, A. K.; de Leeuw, N. H.; Adelung, R. Enhanced UV and ethanol vapour sensing of a single 3-D ZnO tetrapod alloyed with Fe_2O_3 nanoparticles. *Sens. Actuators, B* **2017**, *245*, 448−461.
(11) Yamazoe, N. New approaches for improving semiconductor gas sensors. *Sens. Actuators, B* **1991**, *5*, 7−19.
(12) Lupan, O.; Cretu, V.; Postica, V.; Ahmadi, M.; Cuenya, B. R.; Chow, L.; Tiginyanu, I.; Viana, B.; Pauporté, T.; Adelung, R. Silver-doped zinc oxide single nanowire multifunctional nanosensor with a significant enhancement in response. *Sens. Actuators, B* **2016**, *223*, 893−903.
(13) Lupan, O.; Postica, V.; Marx, J.; Mecklenburg, M.; Mishra, Y. K.; Schulte, K.; Fiedler, B.; Adelung, R. Individual hollow and mesoporous aero-graphitic microtube based devices for gas sensing applications. *Appl. Phys. Lett.* **2017**, *110*, 263109.
(14) Hwang, I.-S.; Choi, J.-K.; Woo, H.-S.; Kim, S.-J.; Jung, S.-Y.; Seong, T.-Y.; Kim, I.-D.; Lee, J.-H. Facile control of C_2H_5OH sensing characteristics by decorating discrete Ag nanoclusters on SnO_2 nanowire networks. *ACS Appl. Mater. Interfaces* **2011**, *3*, 3140−3145.
(15) Joshi, R. K.; Kruis, F. E.; Dmitrieva, O. Gas Sensing Behavior of $SnO_{1.8}$:Ag Films Composed of Size-Selected Nanoparticles. *J. Nanopart. Res.* **2006**, *8*, 797−808.
(16) Shishiyanu, S. T.; Shishiyanu, T. S.; Lupan, O. I. Sensing characteristics of tin-doped ZnO thin films as NO_2 gas sensor. *Sens. Actuators, B* **2005**, *107*, 379−386.
(17) Lupan, O.; Chow, L.; Shishiyanu, S.; Monaico, E.; Shishiyanu, T.; Şontea, V.; Cuenya, B. R.; Naitabdi, A.; Park, S.; Schulte, A. Nanostructured zinc oxide films synthesized by successive chemical solution deposition for gas sensor applications. *Mater. Res. Bull.* **2009**, *44*, 63−69.
(18) Postica, V.; Hölken, I.; Schneider, V.; Kaidas, V.; Polonskyi, O.; Cretu, V.; Tiginyanu, I.; Faupel, F.; Adelung, R.; Lupan, O. Multifunctional device based on ZnO:Fe nanostructured films with enhanced UV and ultra-fast ethanol vapour sensing. *Mater. Sci. Semicond. Process.* **2016**, *49*, 20−33.
(19) Postica, V.; Hoppe, M.; Gröttrup, J.; Hayes, P.; Röbisch, V.; Smazna, D.; Adelung, R.; Viana, B.; Aschehoug, P.; Pauporté, T.; Lupan, O. Morphology dependent UV photoresponse of Sn-doped ZnO microstructures. *Solid State Sci.* **2017**, *71*, 75−86.

DOI: 10.1021/acsami.9b07275
ACS Appl. Mater. Interfaces XXXX, XXX, XXX−XXX

(20) Postica, V.; Vahl, A.; Strobel, J.; Santos-Carballal, D.; Lupan, O.; Cadi-Essadek, A.; de Leeuw, N. H.; Schütt, F.; Polonskyi, O.; Strunskus, T.; Baum, M.; Kienle, L.; Adelung, R.; Faupel, F. Tuning doping and surface functionalization of columnar oxide films for volatile organic compound sensing: experiments and theory. *J. Mater. Chem. A* **2018**, *6*, 23669−23682.
(21) Lupan, O.; Shishiyanu, S.; Ursaki, V.; Khallaf, H.; Chow, L.; Shishiyanu, T.; Sontea, V.; Monaico, E.; Railean, S. Synthesis of nanostructured Al-doped zinc oxide films on Si for solar cells applications. *Sol. Energy Mater. Sol. Cells* **2009**, *93*, 1417−1422.
(22) Vahl, A.; Strobel, J.; Reichstein, W.; Polonskyi, O.; Strunskus, T.; Kienle, L.; Faupel, F. Single target sputter deposition of alloy nanoparticles with adjustable composition via a gas aggregation cluster source. *Nanotechnology* **2017**, *28*, 175703.
(23) Polonskyi, O.; Peter, T.; Mohammad Ahadi, A.; Hinz, A.; Strunskus, T.; Zaporojtchenko, V.; Biederman, H.; Faupel, F. Huge increase in gas phase nanoparticle generation by pulsed direct current sputtering in a reactive gas admixture. *Appl. Phys. Lett.* **2013**, *103*, No. 033118.
(24) Haberland, H.; Karrais, M.; Mall, M.; Thurner, Y. Thin films from energetic cluster impact: A feasibility study. *J. Vac. Sci. Technol., A* **1992**, *10*, 3266−3271.
(25) Lupan, O.; Cretu, V.; Postica, V.; Polonskyi, O.; Ababii, N.; Schütt, F.; Kaidas, V.; Faupel, F.; Adelung, R. Non-planar nanoscale p−p heterojunctions formation in $Zn_xCu_{1-x}O_y$ nanocrystals by mixed phases for enhanced sensors. *Sens. Actuators, B* **2016**, *230*, 832−843.
(26) Lupan, O.; Cretu, V.; Postica, V.; Ababii, N.; Polonskyi, O.; Kaidas, V.; Schütt, F.; Mishra, Y. K.; Monaico, E.; Tiginyanu, I.; Sontea, V.; Strunskus, T.; Faupel, F.; Adelung, R. Enhanced ethanol vapour sensing performances of copper oxide nanocrystals with mixed phases. *Sens. Actuators, B* **2016**, *224*, 434−448.
(27) Cretu, V.; Postica, V.; Mishra, A. K.; Hoppe, M.; Tiginyanu, I.; Mishra, Y. K.; Chow, L.; de Leeuw, N. H.; Adelung, R.; Lupan, O. Synthesis, characterization and DFT studies of zinc-doped copper oxide nanocrystals for gas sensing applications. *J. Mater. Chem. A* **2016**, *4*, 6527−6539.
(28) Kresse, G.; Furthmüller, J. Efficient iterative schemes for ab initio total-energy calculations using a plane-wave basis set. *Phys. Rev. B* **1996**, *54*, 11169−11186.
(29) Hohenberg, P.; Kohn, W. Inhomogeneous Electron Gas. *Phys. Rev.* **1964**, *136*, B864−B871.
(30) Perdew, J. P.; Burke, K.; Ernzerhof, M. Generalized Gradient Approximation Made Simple. *Phys. Rev. Lett.* **1996**, *77*, 3865−3868.
(31) Grimme, S.; Antony, J.; Ehrlich, S.; Krieg, H. A consistent and accurate ab initio parametrization of density functional dispersion correction (DFT-D) for the 94 elements H-Pu. *J. Chem. Phys.* **2010**, *132*, 154104.
(32) Dudarev, S. L.; Botton, G. A.; Savrasov, S. Y.; Humphreys, C. J.; Sutton, A. P. Electron-energy-loss spectra and the structural stability of nickel oxide: An LSDA+U study. *Phys. Rev. B* **1998**, *57*, 1505−1509.
(33) Anisimov, V. I.; Korotin, M. A.; Zaanen, J.; Andersen, O. K. Spin bags, polarons, and impurity potentials in $La_{2-x}Sr_xCuO_4$ from first principles. *Phys. Rev. Lett.* **1992**, *68*, 345−348.
(34) Allen, J. P.; Scanlon, D. O.; Watson, G. W. Electronic structures of silver oxides. *Phys. Rev. B* **2011**, *84*, 115141.
(35) Blöchl, P. E. Projector augmented-wave method. *Phys. Rev. B* **1994**, *50*, 17953−17979.
(36) Watson, G. W.; Kelsey, E. T.; de Leeuw, N. H.; Harris, D. J.; Parker, S. C. Atomistic simulation of dislocations, surfaces and interfaces in MgO. *J. Chem. Soc., Faraday Trans.* **1996**, *92*, 433−438.
(37) Lupan, O.; Postica, V.; Gröttrup, J.; Mishra, A. K.; de Leeuw, N. H.; Carreira, J. F. C.; Rodrigues, J.; Ben Sedrine, N.; Correia, M. R.; Monteiro, T.; Cretu, V.; Tiginyanu, I.; Smazna, D.; Mishra, Y. K.; Adelung, R. Hybridization of Zinc Oxide Tetrapods for Selective Gas Sensing Applications. *ACS Appl. Mater. Interfaces* **2017**, *9*, 4084−4099.
(38) Bader, R. F. W. A quantum theory of molecular structure and its applications. *Chem. Rev.* **1991**, *91*, 893−928.
(39) Chen, J.; Yan, X.; Liu, W.; Xue, Q. The ethanol sensing property of magnetron sputtered ZnO thin films modified by Ag ion implantation. *Sens. Actuators, B* **2011**, *160*, 1499−1503.
(40) Jeong, S. H.; Park, B. N.; Lee, S. B.; Boo, J.-H. Structural and optical properties of silver-doped zinc oxide sputtered films. *Surf. Coat. Technol.* **2005**, *193*, 340−344.
(41) Arguello, C. A.; Rousseau, D. L.; Porto, S. P. S. First-order raman effect in wurtzite-type crystals. *Phys. Rev.* **1969**, *181*, 1351−1363.
(42) Ye, J. D.; Gu, S. L.; Zhu, S. M.; Liu, S. M.; Zheng, Y. D.; Zhang, R.; Shi, Y.; Chen, Q.; Yu, H. Q.; Ye, Y. D. Raman study of lattice dynamic behaviors in phosphorus-doped ZnO films. *Appl. Phys. Lett.* **2006**, *88*, 101905.
(43) Tringe, J. W.; Levie, H. W.; McCall, S. K.; Teslich, N. E.; Wall, M. A.; Orme, C. A.; Matthews, M. J. Enhanced Raman scattering and nonlinear conductivity in Ag-doped hollow ZnO microspheres. *Appl. Phys. A* **2012**, *109*, 15−23.
(44) Shuang, D.; Wang, J. B.; Zhong, X. L.; Yan, H. L. Raman scattering and cathodoluminescence properties of flower-like manganese doped ZnO nanorods. *Mater. Sci. Semicond. Process.* **2007**, *10*, 97−102.
(45) Zeferino, R. S.; Flores, M. B.; Pal, U. Photoluminescence and Raman scattering in Ag-doped ZnO nanoparticles. *J. Appl. Phys.* **2011**, *109*, No. 014308.
(46) Moulder, J. *Handbook of X-ray photoelectron spectroscopy: a reference book of standard spectra for identification and interpretation of XPS data*; Chastain, J. Ed.; Physical Electronics Division, Perkin-Elmer Corporation: Eden Prairie, MN, 1992.
(47) Fan, J.; Freer, R. The roles played by Ag and Al dopants in controlling the electrical properties of ZnO varistors. *J. Appl. Phys.* **1995**, *77*, 4795−4800.
(48) Natsume, Y.; Sakata, H. Zinc oxide films prepared by sol-gel spin-coating. *Thin Solid Films* **2000**, *372*, 30−36.
(49) Natsume, Y.; Sakata, H.; Hirayama, T. Low-temperature electrical conductivity and optical absorption edge of ZnO films prepared by chemical vapour deposition. *Phys. Status Solidi A* **1995**, *148*, 485−495.
(50) Wu, R.-J.; Lin, D.-J.; Yu, M.-R.; Chen, M. H.; Lai, H.-F. Ag@SnO_2 core−shell material for use in fast-response ethanol sensor at room operating temperature. *Sens. Actuators, B* **2013**, *178*, 185−191.
(51) Dua, V.; Surwade, S. P.; Ammu, S.; Agnihotra, S. R.; Jain, S.; Roberts, K. E.; Park, S.; Ruoff, R. S.; Manohar, S. K. All-Organic Vapor Sensor Using Inkjet-Printed Reduced Graphene Oxide. *Angew. Chem., Int. Ed.* **2010**, *122*, 2200−2203.
(52) Chen, H.; Bo, R.; Shrestha, A.; Xin, B.; Nasiri, N.; Zhou, J.; Di Bernardo, I.; Dodd, A.; Saunders, M.; Lipton-Duffin, J.; White, T.; Tsuzuki, T.; Tricoli, A NiO−ZnO Nanoheterojunction Networks for Room-Temperature Volatile Organic Compounds Sensing. *Adv. Opt. Mater.* **2018**, *6*, 1800677.
(53) Choi, K.-I.; Kim, H.-J.; Kang, Y. C.; Lee, J.-H. Ultraselective and ultrasensitive detection of H_2S in highly humid atmosphere using CuO-loaded SnO_2 hollow spheres for real-time diagnosis of halitosis. *Sens. Actuators, B* **2014**, *194*, 371−376.
(54) Power, A. C.; Betts, A. J.; Cassidy, J. F. Silver nanoparticle polymer composite based humidity sensor. *Analyst* **2010**, *135*, 1645−1652.
(55) Thiwawong, T.; Onlaor, K.; Tunhoo, B. A humidity sensor based on silver nanoparticles thin film prepared by electrostatic spray deposition process. *Adv. Mater. Sci. Eng.* **2013**, *2013*, 640428.
(56) Tomer, V. K.; Duhan, S. Ordered mesoporous Ag-doped TiO_2/SnO_2 nanocomposite based highly sensitive and selective VOC sensors. *J. Mater. Chem. A* **2016**, *4*, 1033−1043.
(57) Sysoev, V. V.; Schneider, T.; Goschnick, J.; Kiselev, I.; Habicht, W.; Hahn, H.; Strelcov, E.; Kolmakov, A. Percolating SnO_2 nanowire network as a stable gas sensor: Direct comparison of long-term performance versus SnO_2 nanoparticle films. *Sens. Actuators, B* **2009**, *139*, 699−703.
(58) Mohamad, A. A.; Hassan, M. S.; Yaakob, M. K.; Taib, M. F. M.; Badrudin, F. W.; Hassan, O. H.; Yahya, M. Z. A. First-principles

DOI: 10.1021/acsami.9b07275
ACS Appl. Mater. Interfaces XXXX, XXX, XXX−XXX

calculation on electronic properties of zinc−air system. *J. King Saud Univ., Eng. Sci.* **2017**, *29*, 278−283.
(59) Idrobo, J. C.; Öğüt, S.; Jellinek, J. Size dependence of the static polarizabilities and absorption spectra of Ag_n (n = 2-8) clusters. *Phys. Rev. B* **2005**, *72*, No. 085445.
(60) Lloyd, A. L.; Smith, R.; Kenny, S. D. Critical island size for Ag thin film growth on ZnO (0001$^-$). *Nucl. Instrum. Methods Phys. Res. Sect. B* **2017**, *393*, 22−25.
(61) Duriau, E.; Agouram, S.; Morhain, C.; Seldrum, T.; Sporken, R.; Dumont, J. Growth of Ag thin films on ZnO(000−1) investigated by AES and STM. *Appl. Surf. Sci.* **2006**, *253*, 549−554.
(62) Lin, Z.; Bristowe, P. D. Microscopic characteristics of the Ag(111)/ZnO(0001) interface present in optical coatings. *Phys. Rev. B* **2007**, *75*, 205423.
(63) Hirunsit, P.; Shimizu, K.-i.; Fukuda, R.; Namuangruk, S.; Morikawa, Y.; Ehara, M. Cooperative H_2 Activation at Ag Cluster/θ-Al_2O_3(110) Dual Perimeter Sites: A Density Functional Theory Study. *J. Phys. Chem. C* **2014**, *118*, 7996−8006.
(64) Tarwal, N. L.; Rajgure, A. V.; Patil, J. Y.; Khandekar, M. S.; Suryavanshi, S. S.; Patil, P. S.; Gang, M. G.; Kim, J. H.; Jang, J. H. A selective ethanol gas sensor based on spray-derived Ag−ZnO thin films. *J. Mater. Sci.* **2013**, *48*, 7274−7282.
(65) Sun, Z.-P.; Liu, L.; Zhang, L.; Jia, D.-Z. Rapid synthesis of ZnO nano-rods by one-step, room-temperature, solid-state reaction and their gas-sensing properties. *Nanotechnology* **2006**, *17*, 2266.
(66) Wei, Y.; Wang, X.; Yi, G.; Zhou, L.; Cao, J.; Sun, G.; Chen, Z.; Bala, H.; Zhang, Z. Hydrothermal synthesis of Ag modified ZnO nanorods and their enhanced ethanol-sensing properties. *Mater. Sci. Semicond. Process.* **2018**, *75*, 327−333.
(67) Ding, J.; Zhu, J.; Yao, P.; Li, J.; Bi, H.; Wang, X. Synthesis of ZnO−Ag hybrids and their gas-sensing performance toward ethanol. *Ind. Eng. Chem. Res.* **2015**, *54*, 8947−8953.
(68) Xiang, Q.; Meng, G.; Zhang, Y.; Xu, J.; Xu, P.; Pan, Q.; Yu, W. Ag nanoparticle embedded-ZnO nanorods synthesized via a photochemical method and its gas-sensing properties. *Sens. Actuators, B* **2010**, *143*, 635−640.
(69) Xing, X.; Xiao, X.; Wang, L.; Wang, Y. Highly sensitive formaldehyde gas sensor based on hierarchically porous Ag-loaded ZnO heterojunction nanocomposites. *Sens. Actuators, B* **2017**, *247*, 797−806.
(70) Ma, L.; Ma, S. Y.; Kang, H.; Shen, X. F.; Wang, T. T.; Jiang, X. H. K.; Chen, Q. Preparation of Ag-doped ZnO-SnO2 hollow nanofibers with an enhanced ethanol sensing performance by electrospinning. *Mater. Lett.* **2017**, *209*, 188−192.
(71) Gröttrup, J.; Postica, V.; Smazna, D.; Hoppe, M.; Kaidas, V.; Mishra, Y. K.; Lupan, O.; Adelung, R. UV detection properties of hybrid ZnO tetrapod 3-D networks. *Vacuum* **2017**, *146*, 492−500.

DOI: 10.1021/acsami.9b07275
ACS Appl. Mater. Interfaces XXXX, XXX, XXX−XXX